1 **Localising individual atoms of tryptophan side chains in the metallo-β-lactamase IMP-1**
2 **by pseudocontact shifts from paramagnetic lanthanoid tags at multiple sites**

3 Henry W. Orton,[a,*] Iresha D. Herath,[b,*] Ansis Maleckis,[c] Shereen Jabar,[b] Monika Szabo,[d] Bim
4 Graham,[d] Colum Breen,[e] Lydia Topping,[e] Stephen J. Butler,[e] Gottfried Otting[a]

5

6 [a] ARC Centre of Excellence for Innovations in Peptide & Protein Science, Research School of
7 Chemistry, Australian National University, Canberra, ACT 2601, Australia

8 [b] Research School of Chemistry, The Australian National University, Sullivans Creek Road,
9 Canberra ACT 2601, Australia

10 [c] Latvian Institute of Organic Synthesis, Aizkraukles 21, LV-1006 Riga, Latvia

11 [d] Monash Institute of Pharmaceutical Sciences, Monash University, Parkville, VIC 3052,
12 Australia

13 [e] Department of Chemistry, Loughborough University, Epinal Way, Loughborough, LE11
14 3TU, United Kingdom

18

19 Correspondence: Gottfried Otting (gottfried.otting@anu.edu.au)

20 * These authors contributed equally to this work.

21

22 **Abstract**

23 The metallo-β-lactamase IMP-1 features a flexible loop near the active site that assumes
24 different conformations in single crystal structures, which may assist in substrate binding and
25 enzymatic activity. To probe the position of this loop, we labelled the tryptophan residues of
26 IMP-1 with 7-$^{13}$C-indole and the protein with lanthanoid tags at three different sites. The
27 magnetic susceptibility anisotropy ($\Delta\chi$) tensors were determined by measuring pseudocontact
28 shifts (PCS) of backbone amide protons. The $\Delta\chi$ tensors were subsequently used to identify
29 the atomic coordinates of the tryptophan side chains in the protein. The PCSs were sufficient
30 to determine the location of Trp28, which is located in the active site loop targeted by our
31 experiments, with high accuracy. Its average atomic coordinates showed barely significant
32 changes in response to the inhibitor captopril. It was found that localisation spaces could be
33 defined with better accuracy by including only the PCSs of a single paramagnetic lanthanoid
34 ion for each tag and tagging site. The effect was attributed to the shallow angle with which

35  PCS isosurfaces tend to intersect if generated by tags and tagging sites that are identical except

36  for the paramagnetic lanthanoid ion.

37

38  **1 Introduction**

39  The metallo-β-lactamase IMP-1 is an enzyme that hydrolyses β-lactams, thus conferring

40  penicillin resistance to bacteria. First identified 30 years ago in the Gram-negative bacteria in

41  early 1990s from *Pseudomonas aeruginosa* and *Serratia marcescens* (Bush 2013)*,* IMP-1 has

42  become a serious clinical problem due to horizontal gene transfer by a highly mobile gene

43  ($bla_{IMP-1}$) located on an integron (Arakawa et al., 1995), as the $bla_{IMP-1}$ gene has been detected

44  in isolates of *Klebsiella pneumoniae*, *Pseudomonas putida*, *Alcaligenes xylosoxidans*,

45  *Acinetobacter junii*, *Providencia rettgeri*, *Acinetobacter baumannii* and *Enterobacter*

46  *aerogenes* (Ito et al., 1995; Laraki et al., 1999a; Watanabe et al., 1991). Critically, IMP-1

47  confers resistance also to recent generations of carbapenems and extended-spectrum

48  cephalosporins (Laraki et al., 199b; Bush et al., 2010; van Duin et al., 2013).

49      Multiple crystal structures have been solved of IMP-1, free and in complex with various

50  inhibitors (Concha et al., 2000; Toney et al., 2001; Moali et al., 2003; Hiraiwa et al., 2014;

51  Brem et al., 2016; Hinchliffe et al., 2016; 2018; Wachino et al., 2019; Rossi et al., 2021). IMP-

52  1 belongs to the subclass B1 of metallo-β-lactamases, which contain two zinc ions bridged by

53  the sulfur atom of a cysteine residue in the active site (Concha, 2000). One of $Zn^{2+}$ ions can

54  readily be replaced by a $Fe^{3+}$ ion (Carruthers et al., 2014). The active site is flanked by a loop

55  (referred to as L3 loop) that contains a highly solvent-exposed tryptophan residue surrounded

56  by glycine residues on either side. Both the loop and the tryptophan residue (Trp28 in the IMP-

57  1-specific numbering used by Concha et al. (2000) and Trp64 in the universal numbering

58  scheme by Galleni et al. (2001)) assume different conformations in different crystal structures,

59  suggesting that the loop acts as a mobile flap to cover bound substrate (Fig. 1A). The L3 loop

60  and the functional implication of its flexibility has been studied extensively for different

61  metallo-β-lactamases containing the Gly-Trp-Gly motif in the loop (Huntley et al., 2000; 2003;

62  Moali et al., 2003; Yamaguchi et al., 2015; Palacios et al., 2019; Gianquinto et al., 2020; Softley

63  et al., 2020).  Flexibility of the L3 loop is a general feature also of many metallo-β-lactamases

64  without the Gly-Trp-Gly motif and is thought to contribute to the wide range of β-lactam

65  substrates that can be hydrolyzed by the enzymes (González et al., 2016; Linciano et al., 2019;

66  Salimraj et al., 2018). In the case of the metallo-β-lactamase from *B. fragilis*, which is closely

67  related to IMP-1, electron density could be detected for the Gly-Trp-Gly motif in the crystal

68  structure of the protein in the presence (Payne et al., 2003) but not absence of an inhibitor

69  (Concha et al., 1996), and an NMR relaxation study in solution confirmed the increased

70  flexibility of both the L3 loop and, in particular, the sidechain of the tryptophan residue

71  (Huntley et al., 2000). A similar situation prevails in the case of the IMP-1 variant IMP-13,

72  where different crystal structures of the ligand-free protein show the L3 loop in very different

73  conformations, sometimes lacking electron density, while NMR relaxation measurements

74  confirmed the increased flexibility of the loop (Softley et al., 2020).

75      Due to the rigidity of their sidechains, tryptophan residues frequently contribute to the

76  structural stability of three-dimensional protein folds and it is unusual to observe tryptophan

77  sidechains fully solvent-exposed as in the Gly-Trp-Gly motif of substrate-free IMP-1. The

78  functional role of Trp28 in IMP-1 was assessed in an early mutation study by mutating Trp28

79  to alanine and, in a different experiment, eliminating the L3 loop altogether. Enzymatic activity

80  measurements revealed an increase in the Michaelis constant $K_m$ and a decrease in $k_{cat}/K_m$ ratios

81  for all β-lactams tested, illustrating the importance of the Trp28 sidechain for catalytic activity.

82  Complete removal of the L3 loop reduced the $k_{cat}/K_m$ ratios even further, but without

83  completely abolishing the enzymatic activity (Moali et al., 2003).

84

85



86

3
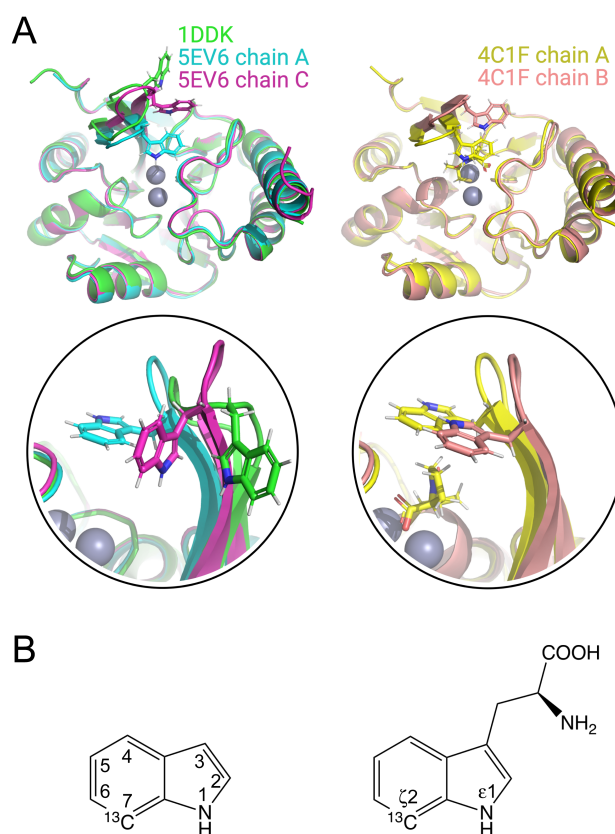
**Figure 1.** Crystal structures of IMP-1 with different conformations of the loop L3 and chemical structures of indole and tryptophan with atom names. (A) Superimposition of crystal structures of IMP-1 highlighting structural variations of Trp28 and the associated loop L3. The structures shown are of the $Zn^{2+}/Zn^{2+}$ complex without inhibitor (green, PDB ID 1DDK, Concha et al., 2000; cyan for chain A and magenta for chain C, PDB ID 5EV6, Hinchliffe et al., 2016), with bound L-captopril (yellow for chain A and salmon for chain B, PDB ID 4CIF, Brem et al., 2016). $Zn^{2+}$ ions are represented by grey spheres and bound captopril is shown in the structure 4C1F chain A. (B) Chemical structures of indole and tryptophan with selected ring positions labelled according to IUPAC conventions. The present work used indole synthesised with a $^{13}C$-$^{1}H$ group in position 7 and deuterium in the ring positions 2, 3, 4, 5 and 6 (Maleckis et al., 2021).

In the crystalline state, the conformation of a solvent-exposed loop is easily impacted by crystal packing forces. Therefore, it is unclear what the actual conformation of the L3 loop is in solution. To address this question, we used solution NMR spectroscopy to assess the location of Trp28 in IMP-1 both in the absence and presence of the inhibitor L-captopril, which inhibits metallo-β-lactamases by binding to the active-site zinc ions (Brem et al., 2016). The analysis was hindered by incomplete backbone resonance assignments of IMP-1 attributed to conformational exchange processes in parts of the protein (Carruthers et al., 2014). As it is difficult to accurately position the atoms of a solvent-exposed polypeptide loop in solution by nuclear Overhauser effects (NOE), we used pseudocontact shifts (PCS) generated by lanthanoid ions attached at different sites of IMP-1 to determine the location of Trp28 relative to the core of the protein. PCSs generated by multiple different paramagnetic metal ions or the same metal ion attached at different sites of a protein have previously been shown to allow localising atoms at remote sites of interest, such as in specific amino acid side chains (Pearce et al., 2017; Lescanne et al., 2018), bound ligand molecules (Guan et al., 2013; Chen et al., 2016) or proteins (Pintacuda et al., 2006; Keizers et al., 2010; de la Cruz et al., 2011; Kobashigawa et al., 2012; Brewer et al., 2015) or for 3D structure determinations of proteins (Yagi et al., 2013; Crick et al., 2015; Pilla et al., 2017).

IMP-1 contains six tryptophan residues, each containing several aromatic hydrogens with similar chemical shifts. To increase the spectral resolution in the 2D NMR spectra recorded for PCS measurements, we labelled each tryptophan sidechain with a single $^{13}C$ atom by expressing the protein in the presence of 7-$^{13}C$-indole (Fig. 1B; Maleckis et al., 2021). The

120    results show that the localisation spaces defined by the tryptophan PCSs fully agree with

121    previously determined crystal structures of IMP-1 for all tryptophan residues. They suggest

122    little change in the average conformation of the L3 loop upon binding of captopril. The results

123    illustrate the accuracy with which the positions of individual atoms can be determined by PCSs

124    from lanthanoid tags even in proteins of limited stability.

125

126    **2 Experimental procedures**

127    **2.1 Production, purification and tagging of proteins**

128    **2.1.1 Plasmid constructs and $^{13}$C-labelled indole**

129    Three different cysteine mutations (A53C, N172C and S204C) were introduced into the $bla_{\text{IMP1}}$

130    gene in the pET-47b(+) plasmid using a modified QuikChange protocol (Qi and Otting, 2019).

131    Deuterated 7-$^{13}$C-indole was synthesized as described with deuteration in all positions other

132    than position 7 (Maleckis et al., 2021). The amino acid sequence of the protein was that

133    reported in the crystal structure 4UAM (Carruthers et al., 2014), except that the N-terminal

134    alanine residue was substituted by a methionine to avoid heterogeneity by incomplete

135    processing by amino peptidase.

136

137    **2.1.2 Protein production**

138    Uniformly $^{15}$N-labelled samples of the cysteine mutants of IMP-1 were expressed in *E. coli*

139    BL21(DE3) cells. The cells were grown at 37 °C in Luria–Bertani (LB) medium containing 50

140    mgL$^{-1}$ kanamycin until the OD$_{600}$ reached 0.6–0.8 and were then transferred to 300 mL of M9

141    medium (6 gL$^{-1}$ Na$_2$HPO$_4$, 3 gL$^{-1}$ KH$_2$PO$_4$, 0.5 gL$^{-1}$ NaCl, pH 7.2) supplemented with 1 gL$^{-1}$

142    of $^{15}$NH$_4$Cl. After induction with isopropyl-β-D-thiogalactopyranoside (IPTG, final

143    concentration 1 mM), the cells were incubated at room temperature for 16 hours. Following

144    centrifugation, the cells were resuspended in buffer A (50 mM HEPES, pH 7.5, 100 µM ZnSO$_4$)

145    for lysis by a homogeniser (Avestin Emulsiflex C5). The supernatant of the centrifuged cell

146    lysate was loaded onto a 5 mL SP column, the column was washed with 20 column volumes

147    buffer B (same as buffer A but with 50 mM NaCl) and the protein was eluted with a gradient

148    of buffer C (same as buffer A but with 1 M NaCl).

149         IMP-1 samples containing 7-$^{13}$C-tryptophan were produced by continuous exchange

150    cell-free protein synthesis (CFPS) from PCR-amplified DNA with eight-nucleotide single-

151    stranded overhangs as described (Wu et al., 2007), using 7-$^{13}$C-indole as a precursor for the *in*

152    *vitro* production of tryptophan (Maleckis et al., 2021). The CFPS reactions were conducted at

153    30 °C for 16 h using 1 mL inner reaction mixture and 10 mL outer buffer. Tryptophan was

154  omitted from the mixture of amino acids provided and deuterated 7-$^{13}$C-indole was added from

155  a stock solution in 50 % DMSO/50 % H$_2$O to the inner and outer buffers at a final concentration

156  of 0.75 mM. The protein samples were purified as described above. About 5 mg of the indole

157  was required for preparing each NMR sample.

158

159  **2.1.3 Ligation with C2-Ln$^{3+}$ tag**

160  To ensure the reduced state of cysteine thiol groups, the protein samples were treated with 2

161  mM dithiothreitol (DTT) for 1 hour. Subsequently, the DTT was removed using an Amicon

162  ultrafiltration centrifugal tube with a molecular weight cut-off of 10 kDa, concentrating the

163  protein samples to 50 μM in buffer A. The samples were incubated overnight at room

164  temperature with shaking in the presence of five-fold molar excess of C2 tag (Graham et al.,

165  2011; de la Cruz et al., 2011) loaded with either Y$^{3+}$, Tb$^{3+}$ or Tm$^{3+}$. Following the tagging

166  reaction, the samples were washed using an Amicon centrifugal filter unit to remove unbound

167  tag and the buffer was exchanged to NMR buffer (20 mM MES, pH 6.5, 100 mM NaCl).

168

169  **2.1.4 Ligation with C12-Ln$^{3+}$ tag**

170  The ligation reaction of IMP-1 N172C with the C12-Ln$^{3+}$ tag loaded with either Y$^{3+}$, Tb$^{3+}$ or

171  Tm$^{3+}$ (Herath et al., 2021) was conducted in the same way as with the C2-Ln$^{3+}$ tags, except that

172  the reactions were carried out in buffer A with the pH adjusted to 7.0.

173

174  **2.2 NMR spectroscopy**

175  All NMR data were acquired at 37 °C on Bruker 600 and 800 MHz NMR spectrometers

176  equipped with TCI cryoprobes designed for 5 mm NMR tubes, but only 3 mm NMR tubes were

177  used in this project. Protein concentrations were 0.6 mM and 0.2 mM for $^{15}$N-HSQC spectra

178  of samples labelled with the C2 and C12 tag, respectively. The protein concentrations were 0.4

179  mM for $^{13}$C-HSQC and NOE-relayed $^{13}$C-HSQC spectra. $^{15}$N-HSQC spectra were recorded at

180  a $^1$H-NMR frequency of 800 MHz with $t_{1max}$ = 40 ms, $t_{2max}$ = 170 ms, using a total recording

181  time of 3 h per spectrum. $^{13}$C-HSQC spectra were recorded with a S$^3$E filter to select the low-

182  field doublet component due to the $^1J_{HC}$ coupling of the $^{13}$C-labelled tryptophan side chains.

183  The pulse sequence is shown in Fig. S9 and the spectra were recorded at a $^1$H-NMR frequency

184  of 600 MHz using $t_{1max}$ = 20–50 ms, $t_{2max}$ = 106 ms and total recording times of 2 h per

185  spectrum. $^{13}$C-HSQC spectra with NOE relay were recorded without decoupling in the $^{13}$C-

186  dimension, relying on relaxation and $^{13}$C equilibrium magnetisation to emphasize the narrow

187  doublet component. The NOE mixing time was 150 ms and the total recording time 3 h per
188  spectrum. The pulse sequence is shown in Fig. S10.
189      To account for uncertainties in concentration measurements, samples with L-captopril
190  were prepared with a nominal ratio of captopril to protein of 1.5:1. In the case of samples
191  tagged with the C2 tag, however, this lead to gradual release of some of the tag, as captopril
192  contains a free thiol group and the disulfide linkage of the C2 tag is sensitive to chemical
193  reduction. To limit this mode of sample degradation, the NOE-relayed $[^{13}C,^{1}H]$-HSQC spectra
194  were recorded with a smaller excess of captopril.
195

196  **2.3 Δχ-tensor fits**
197  The experimental PCSs ($\Delta\delta^{PCS}$) were measured in ppm as the amide proton chemical shift
198  observed in NMR spectra recorded for the IMP-1 mutants A53C, N172C and S204C tagged
199  with $Tm^{3+}$ or $Tb^{3+}$ tags minus the corresponding chemical shift measured of samples made with
200  $Y^{3+}$ tags. The resonance assignments of the wild-type $Zn_2$ enzyme (BMRB entry 25063) were
201  used to assign the $^{15}N$-HSQC cross-peaks in the diamagnetic state. The program Paramagpy
202  (Orton et al., 2020) was used to fit magnetic susceptibility anisotropy ($\Delta\chi$) tensors to crystal
203  structures of IMP-1 solved in the absence and presence of the inhibitor captopril.
204

205  **3 Results**
206  **3.1 Protein production**
207  Three cysteine mutants of uniformly $^{15}N$-labelled IMP-1 were produced *in vivo*, where cysteine
208  residues replaced Ala53, Asn172 and Ser204, respectively. The purified proteins were tagged
209  with C2 tags containing $Tb^{3+}$ or $Tm^{3+}$ as the paramagnetic ions and $Y^{3+}$ as the diamagnetic
210  reference. Samples of the uniformly $^{15}N$-labelled mutant N172C were also ligated with C12
211  tags containing the same set of metal ions. The chemical structures of the tags are depicted in
212  Fig. S1. To record $^{13}C$-$^{1}H$ correlation spectra of the tryptophan side chains with minimal
213  spectral overlap, additional samples of the cysteine mutants were produced with selectively
214  $^{13}C$-labelled tryptophan residues. These samples were produced by cell-free protein synthesis
215  in the presence of 7-$^{13}C$ indole, deuterated except at the 7 position, with the omission of
216  tryptophan, using a recently established protocol (Maleckis et al., 2021). The residual activity
217  of tryptophan synthase in the cell-free extract was sufficient to produce tryptophan from the
218  added $^{13}C$-labelled indole. The resulting tryptophan residues contained a $^{13}C$-$^{1}H$ group in
219  position 7 ($^{13}C^{\zeta 2}$ and $^{1}H^{\zeta 2}$ in IUPAC nomenclature; Markley et al., 1998) and deuterons at all

220 other hydrogen positions of the indole ring except for the $H^N$ atom ($H^{\varepsilon 1}$ in IUPAC

221 nomenclature). The cell-free expression yielded about 2 mg of purified protein per millilitre of

222 inner cell-free reaction mixture. Mass spectrometry indicated that the tryptophan residues of

223 IMP-1 were $^{13}C/^2H$-labelled with about 80 % labelling efficiency at each of the six tryptophan

224 positions (Fig. S2). The purified proteins were ligated with C2-$Ln^{3+}$ tags containing either $Tb^{3+}$,

225 $Tm^{3+}$ or $Y^{3+}$ as in the case of the $^{15}N$-labelled samples. Ligation yields with the C2 tags were

226 practically complete as indicated by mass spectrometry (Fig. S2). The ligation yield of the

227 N172C mutant with C12 tags was about 90 % (Herath et al., 2021).

228

**3.2 NMR experiments and resonance assignments**

230 [$^{15}N,^1H$]-HSQC spectra were measured of the tagged proteins in the free state and in the

231 presence of L-captopril (Fig. S3–S8). $^1H$ PCSs of backbone amide protons measured in these

232 spectra were used to establish the $\Delta\chi$ tensors relative to the protein. The resonance assignment

233 of the [$^{15}N,^1H$]-HSQC spectra in the presence of inhibitor was transferred from the

234 corresponding spectra recorded in the absence of inhibitor. As no resonance assignments could

235 reliably be made in this way in areas of spectral overlap, fewer resonance assignments were

236 available in the presence than absence of inhibitor. Furthermore, due to captopril releasing

237 some of the C2 tags from the protein by breaking the disulfide bridge of the tag attachment,

238 spectra recorded in the presence of captopril contained additional cross-peaks from

239 diamagnetic protein.

240 To obtain tagged protein that is inert against chemical reduction, we also attached the

241 C12 tag to the mutant N172C. This tag, however, caused the appearance of additional peaks in

242 the [$^{15}N,^1H$]-HSQC spectra (Fig. S7). The additional peaks appeared in different sample

243 preparations, indicating sample degradation or perturbation of the local protein structure by the

244 tag. We therefore based the rest of the work mainly on the PCSs obtained with the C2 tags.

245 Tables S1 and S2 list the PCSs of the backbone amides measured in the absence and presence

246 of captopril.

247 $^1H$ PCSs of the tryptophan $H^{\zeta 2}$ protons were measured in [$^{13}C,^1H$]-HSQC spectra

248 recorded with $S^3E$ spin-state selection element (Meissner et al., 1997) in the $^{13}C$ dimension to

249 select the slowly relaxing components of the doublets split by $^1J_{HC}$ couplings. Cross-peaks were

250 observed for all six tryptophan residues except for the mutant N172C, which displayed cross-

251 peaks of only five tryptophan indoles (Fig. 2). The missing signal was attributed to Trp176

252 because of its close proximity to the tagging site. The indole $H^{\varepsilon 1}$ proton is located within 2.9 Å

253   of the $H^{\zeta 2}$ proton and the NOE between both protons was readily observed in a $[^{13}C,^{1}H]$-HSQC

254   experiment with NOE relay (Fig. 2). The $H^{\varepsilon 1}$ chemical shifts afforded better spectral resolution

255   than the $H^{\zeta 2}$ resonances. Comparison of the predicted and observed PCSs yielded resonance

256   assignments of all tryptophan $H^{\varepsilon 1}$ cross-peaks with particular clarity in the NOE-relayed

257   $[^{13}C,^{1}H]$-HSQC spectrum (Fig. 2). In addition, the assignment was supported by paramagnetic

258   relaxation enhancements (for example, Trp88 is near residue 53 and therefore its cross-peaks

259   were strongly attenuated in the paramagnetic samples of the A53C mutant). Different PCSs

260   were observed for all six tryptophan sidechains and different PCSs were observed for the $H^{\zeta 2}$

261   and $H^{\varepsilon 1}$ protons within the same indole sidechain. Each of the tryptophan sidechains showed

262   PCSs in most, if not all, of the mutants. As the L3 loop is near residue 172, the mutant N172C

263   endowed Trp28 with particularly large PCSs. Tables S3 and S4 report the PCSs measured in

264   this way for the samples labelled with C2 tags.

265        In contrast, assigning the indole N-H groups in the $[^{15}N,^{1}H]$-HSQC spectra was much

266   more difficult because IMP-1 is a protein prone to showing more than a single peak per proton

267   (Figs S5 and S6). In particular, the $[^{15}N,^{1}H]$-HSQC spectrum of wild-type IMP-1 selectively

268   labelled with $^{15}N$-tryptophan displayed six intense and at least three weak $N^{\varepsilon 1}$–$H^{\varepsilon 1}$ cross-peaks

269   (Fig. S6; Carruthers et al., 2014) and the $[^{15}N,^{1}H]$-HSQC spectra of the tagged cysteine mutants

270   showed evidence of heterogeneity too (Fig. S5). Nonetheless, the six most intense $N^{\varepsilon 1}$–$H^{\varepsilon 1}$

271   cross-peaks could be assigned by comparison to the PCSs observed in the NOE-relayed

272   $[^{13}C,^{1}H]$-HSQC spectrum and this assignment was used to measure the PCSs of the tryptophan

273   $H^{\varepsilon 1}$ resonances in the mutant N172C tagged with C12 tag (Fig. S8; Table S4).

274        Spectra recorded in the presence of L-captopril were very similar to those recorded

275   without the inhibitor, except that some new, narrow C-H cross-peaks appeared in the $[^{13}C,^{1}H]$-

276   HSQC spectra of the mutants A53C and S204C, which were suggestive of protein degradation

277   (Fig. 3). We consequently used the better-resolved indole $H^N$ cross-peaks to identify the correct

278   parent C-H cross-peaks. The chemical shifts of the tryptophan sidechains changed very little

279   in response to the presence of L-captopril, except for the $^{13}C$-chemical shift of Trp28, which is

280   nearest to the ligand binding site. The PCSs of the indole protons measured in the presence of

281   the inhibitor are listed in Tables S5 and S6.

282

283   **3.2 $\Delta\chi$-tensor fits**

284   The $\Delta\chi$-tensor parameters were determined using the program Paramagpy (Orton et al., 2020),

285   using all available $^{1}H$ PCSs measured of backbone amides. Comparing the $\Delta\chi$ tensor fits to the

286     crystal structures 5EV6 chains A and C (Hinchliffe et al., 2016) and 1DDK (Concha et al.,

287     2000) of the free protein, the chain A of the structure 5EV6 proved to produce the smallest $Q$

288     factor by a small margin (Fig. S11) and was used as the reference structure of the free protein

289     for the subsequent evaluation. Similarly, chain A of the co-crystal structure published with the

290     inhibitor L-captopril (PDB ID: 4C1F; Brem et al., 2016) on average delivered better fits than

291     chain B and was used as the reference structure for the NMR data recorded in the presence of

292     L-captopril. The $\Delta\chi$-tensor fits of each mutant and tag used a common metal position for the

293     data obtained with the $Tb^{3+}$ and $Tm^{3+}$ tags. The fits positioned the paramagnetic centres at

294     distances between 8.2 and 9.4 Å from the $C^\beta$ atom of the tagged cysteine residues, which is

295     compatible with the chemical structure of the C2-tag. Figure 4 shows the correlations between

296     back-calculated and experimental PCSs and Table S7 reports the fitted $\Delta\chi$ tensor parameters.

297     Very similar $Q$ factors were obtained when using the PCSs measured in the absence of inhibitor

298     to fit the $\Delta\chi$ tensor to the co-crystal structure 4C1F or the PCSs measured in the presence of

299     inhibitor to fit the $\Delta\chi$ tensor to the crystal structure of the free protein. This indicates that the

300     protein structure did not change very much in response to inhibitor binding. This conclusion

301     was also indicated by the similarity between the backbone PCSs observed with and without

302     inhibitor (Fig. S12).

303        The $\Delta\chi$ tensors obtained with the $Tb^{3+}$ tags were larger than those obtained with the

304     $Tm^{3+}$ tags, which is also reflected by the consistently larger PCSs observed in the $^{13}C$-$^1H$

305     correlation spectra of Fig. 2 and 3. The fits of $\Delta\chi$ tensors to the protein backbone also yielded

306     better $Q$ factors for PCSs generated by $Tb^{3+}$ than $Tm^{3+}$ ions. Therefore, we determined the

307     localisation spaces of the tryptophan sidechains in the first instance by using their $^1H$ PCSs

308     measured with $Tb^{3+}$ tags only.

309
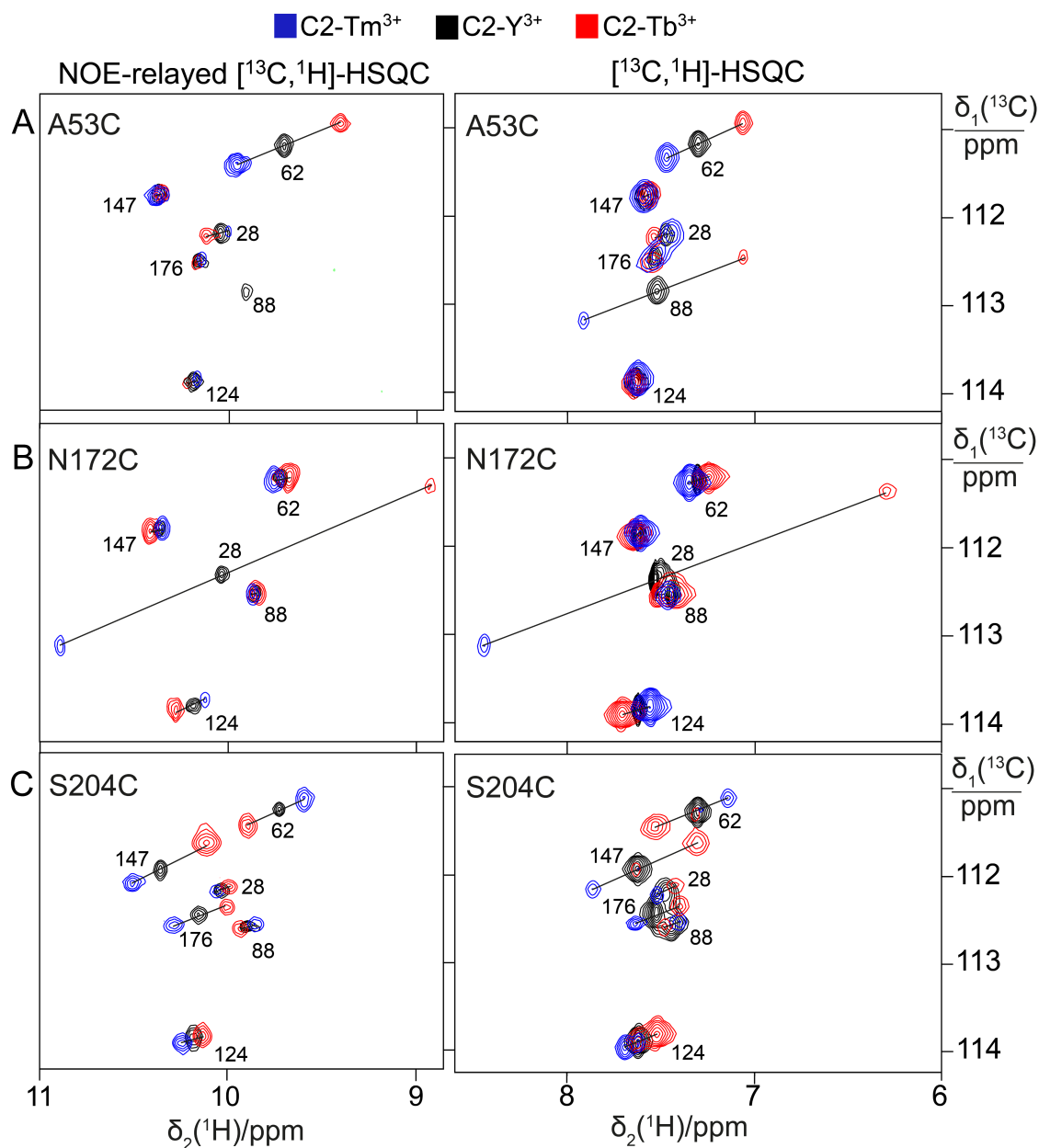
**Figure 2.** PCSs observed in $^{13}C$-$^1H$ correlation spectra of 0.4 mM solutions of IMP-1 mutants tagged with C2-$Ln^{3+}$ tags and containing selectively isotope-labelled tryptophan produced from 7-$^{13}C$-indole deuterated in the positions 2, 4, 5 and 6. The plots show superimpositions of spectra recorded with diamagnetic (C2-$Y^{3+}$, black) or paramagnetic (C2-$Tb^{3+}$, red; C2-$Tm^{3+}$, blue) tags. All spectra were recorded with spin-state selection in the $^{13}C$-dimension to record the narrow low-field component of each $^{13}C$-doublet. Right panels: [$^{13}C$,$^1H$]-HSQC spectra. Left panels: NOE-relayed [$^{13}C$,$^1H$]-HSQC spectra (150 ms NOE mixing time) to record the $H^{\varepsilon 1}$ resonances of the tryptophan side chains. PCSs are indicated by lines connecting the peaks of paramagnetic and diamagnetic samples. The cross-peaks are assigned with the residue number of the individual tryptophan residues. (A) Mutant A53C. (B) Mutant N172C. (C) Mutant
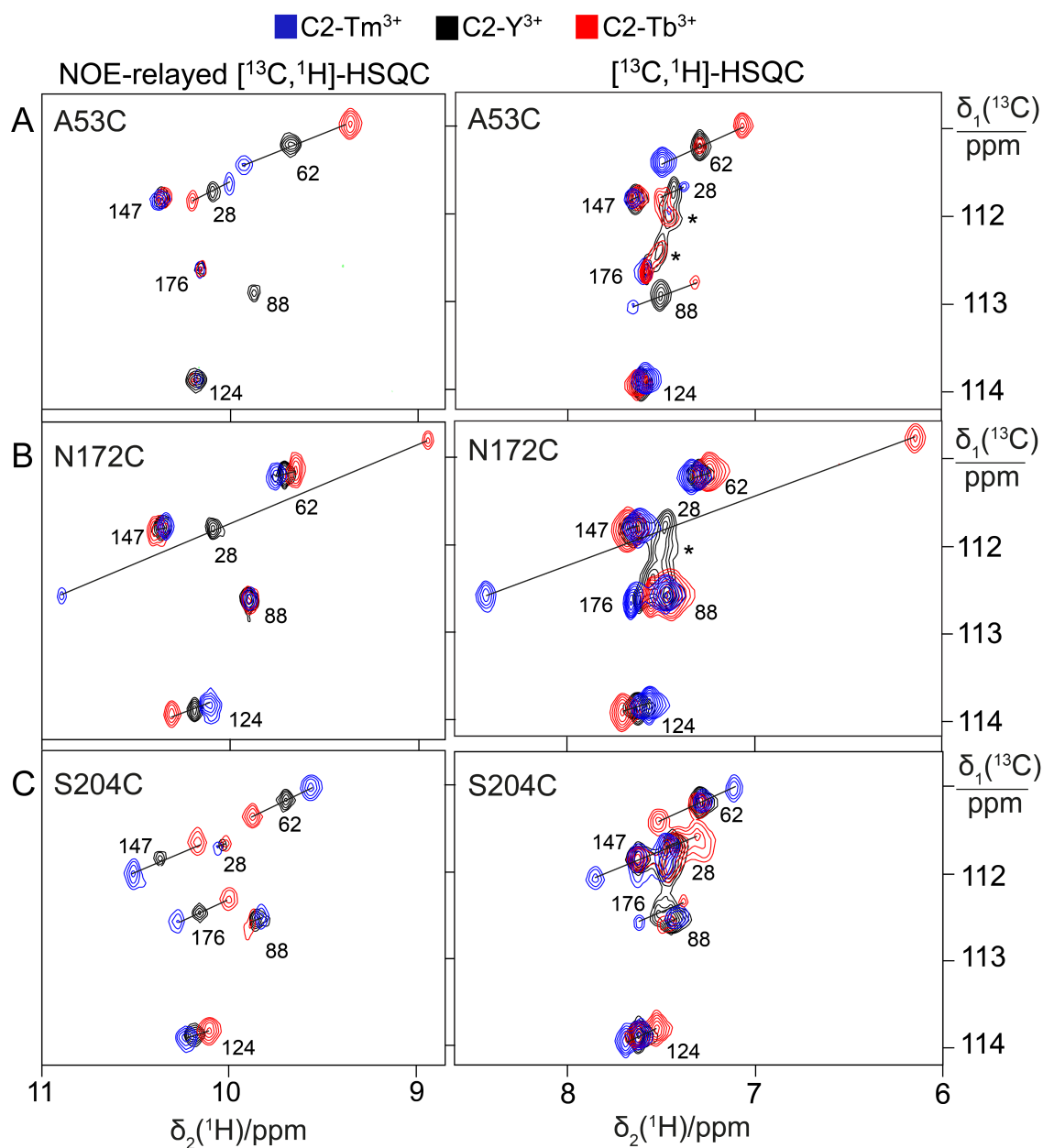
**Figure 3.** Effect of the presence of L-captopril on the PCSs observed in $^{13}C$-$^1H$ correlation spectra of 0.4 mM solutions of IMP-1 mutants. Protein preparations and experimental parameters were the same as in Fig. 2. Spectra recorded with diamagnetic (C2-Y$^{3+}$, black) or paramagnetic (C2-Tb$^{3+}$, red; C2-Tm$^{3+}$, blue) tags are superimposed. Right column: [$^{13}C$,$^1H$]-HSQC spectra. Left column: NOE-relayed [$^{13}C$,$^1H$]-HSQC spectra recorded with150 ms NOE mixing time. Stars mark cross-peaks of species putatively attributed to protein degradation. (A) Mutant A53C. (B) Mutant N172C. (C) Mutant S204C.
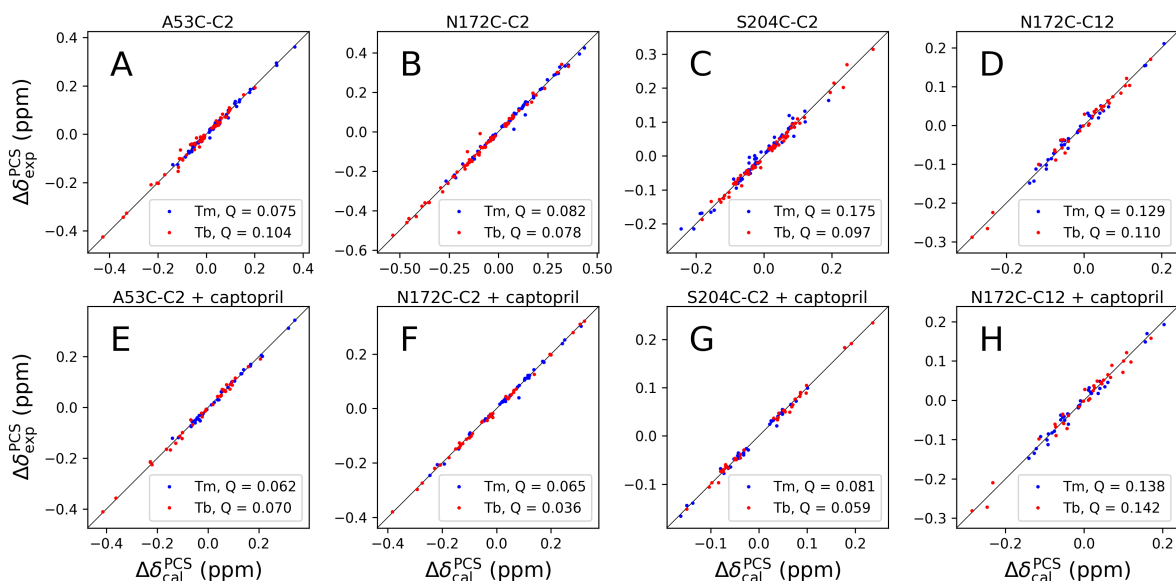
**Figure 4.** Correlations between back-calculated and experimental $^1$H PCSs measured of backbone amides of IMP-1 with C2 tags at three different sites (positions 53, 172 and 204) and the C12 tag in position 172. Red and blue data points correspond to the PCS data obtained with Tb$^{3+}$ and Tm$^{3+}$ tags, respectively. (A) Mutant A53C with C2 tag. (B) Mutant N172C with C2 tag. (C) Mutant S204C with C2 tag. (D) Mutant N172C with C12 tag. (E) Same as (A) but in the presence of captopril. (F) Same as (B) but in the presence of captopril. (G) Same as (C) but in the presence of captopril. (H) Same as (D) but in the presence of captopril. PCS data in (A)–(D) were used to fit $\Delta\chi$ tensors to the structure 5EV6. PCS data in (E)–(F) were used to fit $\Delta\chi$ tensors to the structure 4C1F.

### 3.3 Determining the localisation spaces of tryptophan sidechains

The $\Delta\chi$ tensors determined of backbone amides not only enabled the resonance assignment of the tryptophan sidechains by comparing back-calculated with experimental PCSs, but also allowed translation of the indole PCSs into restraints that define the locations of the tryptophan H$^{\zeta 2}$ and H$^{\varepsilon 1}$ atoms with respect to the rest of the protein. The concept of localising nuclear spins by PCSs that are generated by lanthanoid tags at different sites is well-established (see, e.g., Yagi et al., 2013; Lescanne et al., 2018; Zimmermann et al., 2019). It can be visualised by representing each PCS restraint by the corresponding PCS isosurface, which comprises all points in space where this PCS value is generated by the $\Delta\chi$ tensor (Fig. 5). With PCS restraints from two different metal sites, the intersection between the respective isosurfaces defines a line. The intersection of this line with the PCS isosurface from a third $\Delta\chi$ tensor defines two points. While a fourth $\Delta\chi$ tensor could unambiguously produce a single solution, a fourth tensor

13

355  may not be required if one of these two points is incompatible with the covalent structure of

356  the protein. In favourable circumstances, the constraints imposed by the covalent structure may

357  even allow the accurate positioning of nuclear spins by PCSs generated from only two different

358  $\Delta\chi$ tensors (Pearce et al., 2017). Therefore, the present study was successful with only three

359  different tagging sites. Figure S13 illustrates the concept for the Trp28 $H^{\varepsilon 1}$ atom.

360      The spatial definition of the intersection point defined by the PCS isosurfaces depends

361  on the experimental uncertainties in a non-isotropic way, as the PCS isosurfaces rarely intersect

362  in an orthogonal manner and the PCS gradients differ for each $\Delta\chi$ tensor. To capture a

363  localisation space, which allows for the experimental uncertainty in the measured PCS data,

364  we mapped the spatial field of root-mean-squared deviations (RMSD) between experimental

365  and calculated PCS values and defined the boundary of the localisation space by a maximal

366  RMSD value. In addition, uncertainties in the $\Delta\chi$ tensors were propagated by averaging over

367  the results from 20 $\Delta\chi$-tensor fits performed with random omission of 20 % of the backbone

368  PCS data. In the present work, the routine for defining the localisation space was implemented

369  as a script in the software Paramagpy (Orton et al., 2020). Figure 6 shows the resulting

370  localisation spaces for the $H^{\varepsilon 1}$ and $H^{\zeta 2}$ atoms of Trp28, using the PCS data obtained for the

371  three cysteine mutants A53C, N172C and S204C with the C2-$Tb^{3+}$ tag as well as the N172C

372  mutant with the C12-$Tb^{3+}$ tag.

373      The localisation spaces found for the $H^{\varepsilon 1}$ and $H^{\zeta 2}$ atoms of Trp28 were clearly different.

374  Furthermore, the distance between them corresponded closely to the distance expected from

375  the chemical structure of the indole ring (2.9 Å). The irregular shapes of the localisation spaces

376  displayed in Fig. 6 purely reflect the relative geometry of the intersecting PCS isosurfaces and

377  do not take into account any dynamic flexibility of the L3 loop or protein structure. In

378  particular, the relevant PCS isosurfaces associated with the C2 tag at sites N172C and S204C

379  intersect at a shallow angle, which leads to the elongated shape of the localisation space for the

380  Trp28 $H^{\zeta 2}$ atom (Fig. S13). For the nitrogen-bound $H^{\varepsilon 1}$ atom, the localisation space was

381  restricted further by the additional data obtained with the C12 tag at site N172C (Fig. 6).

382  Calculating the localisation spaces from the $Tm^{3+}$ data yielded very similar results (Fig. S14).

383  The agreement of the localisation spaces of Trp28 with chain A of the previously published

384  crystal structure 5EV6 is excellent and they are clearly incompatible with the conformations

385  observed in chain C of the same structure or in the structure 1DDK (Fig. 1A).

386      Due to close proximity to the C2 tags in the N172C mutant, the largest PCSs were

387  observed for Trp28 $H^{\varepsilon 1}$ but, in the absence of captopril, their exact magnitude appeared about

388  0.3 ppm smaller in the $[^{15}N,{}^{1}H]$-HSQC (Fig. S5b) than the NOE-relayed $[^{13}C,{}^{1}H]$-HSQC (Fig.

389  2B) spectrum. The centre of the localisation space of Trp28 $H^{\varepsilon 1}$ moved to a slightly more open

390  L3 loop conformation when using the smaller PCS detected in the $[^{15}N,{}^{1}H]$-HSQC spectrum

391  of the N172C mutant labelled with the C2-$Tb^{3+}$ tag. The space still encompassed the

392  coordinates observed in the structure 5EV6, limiting the significance of this difference in PCS.

393      None of the minor additional cross-peaks observed in any of the sample preparations

394  could be attributed to alternative conformations of Trp28 either. In particular, the most extreme

395  conformation observed in the crystal structure 1DDK (green in Fig. 1) predicts PCSs > 1 ppm

396  for Trp28 $H^{\varepsilon 1}$ in the mutant N172C with C2 tags, but we observed no PCS of this magnitude

397  for any of the unassigned peaks.

398

399

400  **3.4 Defining the localisation space with one versus two lanthanoid ions in the same tag**

401  **and at the same site**

402  Unexpectedly, determining separate localisation spaces from the $Tm^{3+}$ and $Tb^{3+}$ datasets

403  yielded more plausible results than when both datasets were used simultaneously. Careful

404  inspection showed that the close alignment of the $\Delta\chi$ tensors of the $Tm^{3+}$ and $Tb^{3+}$ data resulted

405  in particularly shallow intersection angles of the respective PCS isosurfaces. In calculating the

406  localisation space of Trp28, the PCS isosurfaces arising from the N172C mutant carried by far

407  the greatest weight as this site is closer to residue 28 than the sites 53 and 204. Therefore, the

408  $Tm^{3+}$ and $Tb^{3+}$ data from the N172C mutant dominated the PCS RMSD calculation and the

409  intersection between the associated isosurfaces pulled the final localisation space to a

410  structurally implausible location, which was unstable with respect to small perturbations in $\Delta\chi$-

411  tensor orientations associated with the tensors at site 172. In contrast, considering the $Tm^{3+}$ and

412  $Tb^{3+}$ datasets separately allowed the localisation spaces to be determined by the intersections

413  with PCS isosurfaces from the other sites. The resulting localisation spaces consistently were

414  compatible with crystal structures.

415

416
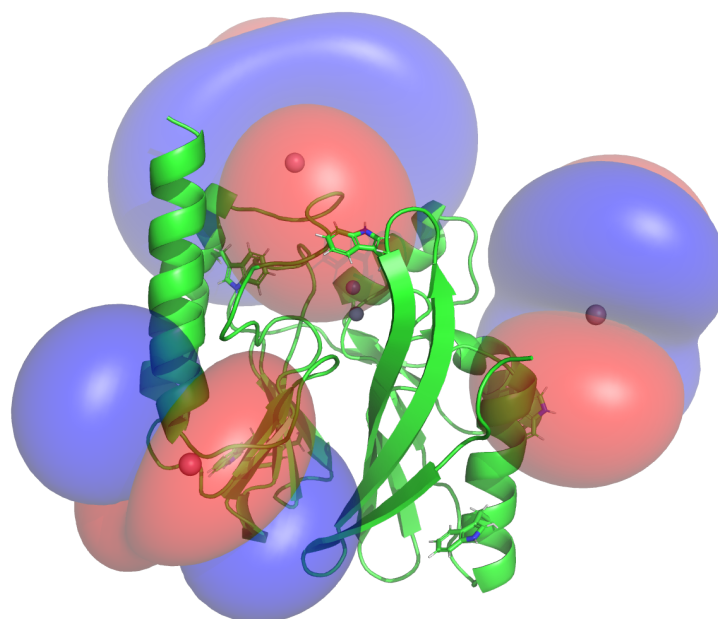
**Figure 5.** PCS isosurfaces of the IMP-1 mutants A53C, N172C and S204C plotted on the crystal structure 5EV6. The respective $\Delta\chi$ tensors were determined from the $^1$H PCSs measured of backbone amides. Blue/red isosurfaces correspond to PCSs of +/-1.0 ppm, respectively, generated with C2-Tb$^{3+}$ tags.

421



422
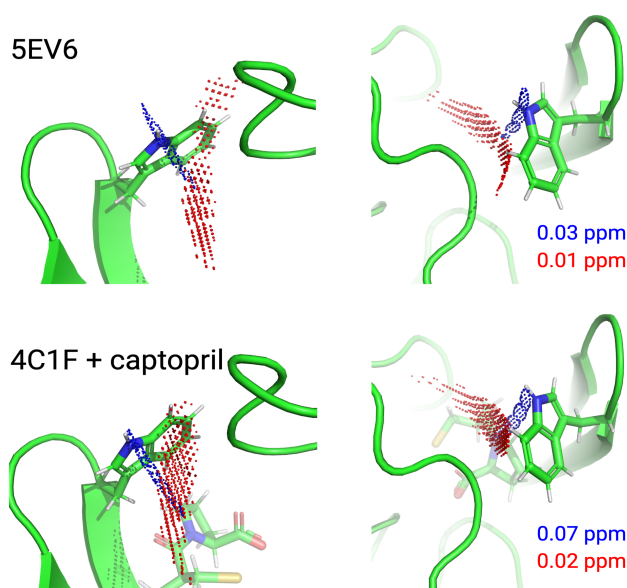
**Figure 6.** Localisation space of the sidechain of Trp28 defined by the PCSs from tags in the IMP-1 mutants A53C, N172C and S204C. The left and right panels display the same results in two different orientations. Red and blue points outline localisation spaces determined for the H$^{\zeta 2}$ and H$^{\epsilon 1}$ atoms, respectively. The localisation space of the H$^{\zeta 2}$ atom was defined by the PCSs and $\Delta\chi$ tensors determined for the Tb$^{3+}$-loaded C2 tags, while the localisation space of the H$^{\epsilon 1}$ atom was restricted by additional data obtained with C12-Tb$^{3+}$ tag at site N172C. The

429   boundaries of the respective localisation spaces displayed are defined by the PCS RMSD values

430   indicated in ppm. The top panel depicts the localisation spaces determined for the free protein

431   plotted on chain A of the crystal structure 5EV6 depicted in two different orientations. The

432   lower panel depicts the localisation spaces determined in the presence of captopril plotted on

433   chain A of the crystal structure 4C1F.

434

435   **3.5 L3 loop conformation in the presence of L-captopril**

436   Figure 6 shows that, within the uncertainty of the experiments, the localisation space of the

437   indole sidechain of Trp28 is invariant with respect to the presence or absence of captopril.

438   Conservation of the L3 loop conformation with and without inhibitor is supported by the close

439   similarity in all the PCSs observed for Trp28 in the NOE-relayed $[^{13}C,^{1}H]$-HSQC spectra (Fig.

440   2 and 3). In the $[^{1}H,^{15}N]$-HSQC spectra of the mutant N172C with C2 tag, however, the PCSs

441   observed for Trp28 H$^{\varepsilon 1}$ appeared somewhat smaller without than with captopril (Fig. S5b). As

442   the PCSs of backbone amides were very similar in the absence and presence of the inhibitor

443   (Fig. S12), this difference in PCS suggests a change in L3 loop conformation, contradicting the

444   observations made with the selectively $^{13}C$-labelled samples. As discussed above, using the

445   smaller PCS of Trp28 H$^{\varepsilon 1}$ did not sufficiently change its localisation space in the free protein

446   to render it incompatible with the coordinates of the structure 5EV6. Therefore, as far as the

447   data of the $^{15}N$-labelled samples indicate a conformational change of the L3 loop between the

448   free and bound state, it is small. We attribute the differences in PCSs observed between the

449   selectively $^{13}C$-labelled and uniformly $^{15}N$-labelled samples to differences in sample

450   preparation of unknown origin, which are also reflected by different numbers of weak

451   unassigned cross-peaks (Figs 2, 3, S5 and S6).

452       The cross-peak intensities of the Trp28 sidechain resonances are relatively weak

453   compared with those of the other tryptophan sidechains, suggesting that Trp28 is subject to

454   dynamics that broaden its resonances. Its cross-peaks appeared slightly weaker in the presence

455   than in the absence of inhibitor (Fig. 2 and 3), suggesting a change in dynamics caused by the

456   inhibitor binding. Previous NMR studies of metallo-β-lactamases reported faster $R_2(^{15}N)$

457   relaxation rates of the L3-loop tryptophan sidechain in the presence than in the absence of

458   inhibitor, which was attributed to dampened dynamics (Huntley et al., 2000; Softley et al.,

459   2020). In the presence of dynamics, the localisation spaces determined in the present work

460   must be considered averages that do not report on the amplitude or direction of motions.

461

**3.6 Localisation spaces of tryptophan side chains other than Trp28**

As the tagging sites had been designed to analyse the conformation of the L3 loop, they were positioned at similar distances from the L3 loop and therefore not optimal for determining localisation spaces of the other tryptophan residues. Nonetheless, clear differences were observed in the PCSs of the $H^{\xi 2}$ and $H^{\varepsilon 1}$ atoms (Fig. 2), allowing the separation of the respective localisation spaces, which also proved to be in excellent agreement with the conformations of the side-chain indoles of Trp62, Trp124 and Trp147 as found in the crystal structure (Fig. S15), whereas the data were insufficient to determine the sidechain conformation of Trp176.

**4 Discussion**

The L3 loop of metallo-β-lactamases is known to be flexible and, in the specific case of IMP-1, significantly assists in substrate binding and enzymatic activity (Moali et al., 2003). As the substrate is sandwiched between the di-zinc site and the L3 loop, it is tempting to think that the loop opens up for substrate binding and product release while it may be closed during the enzymatic reaction to hold the substrate and reaction intermediate in place. In contrast, some of the conformations observed in crystal structures of IMP-1 obtained in the presence and absence of the inhibitor ʟ-captopril, revealed the loop in almost identical conformations (Brem et al., 2016). This observation is inconclusive, however, as the L3 loop forms more extensive intermolecular contacts with neighbouring protein molecules in the crystal lattice than intramolecular contacts. In addition, other crystal structures observed the loop to move by almost 3 Å in response to a different inhibitor (Concha et al., 2000). This prompted us to probe its actual location in the absence of crystal packing forces in solution, a task which is difficult to tackle by traditional NMR spectroscopic methods that rely on short-range NOEs.

Our results show that by furnishing IMP-1 with paramagnetic lanthanoid tags, the coordinates of the indole sidechain of Trp28, which is a key residue near the tip of the loop, can be determined with remarkable accuracy even in the free protein, where the available crystal structures position the L3 loop in a conformation without any direct contacts with the core of the protein. Indeed, the localisation space identified by the NMR data of the free protein proved to be sufficiently well-defined to discriminate between different crystal structures of IMP-1, as well as between different chains in the same asymmetric crystal unit. For example, the sidechain orientation of Trp28 observed in $[Fe^{3+}, Zn^{2+}]$-IMP-1 (4UAM; Carruthers et al., 2014) proved to be in poor agreement with the PCS data, whereas the data were in full agreement with chain A in the structure 5EV6 of $[Zn^{2+}, Zn^{2+}]$-IMP-1 without inhibitor

495    (Hinchliffe et al., 2016) and chain A in the structure 4C1F with bound L-captopril (Brem et al.,

496    2016). This highlights the outstanding capacity of PCSs to assess small conformational

497    differences.

498          The approach of using PCSs for local structure determination is particularly appealing

499    in the case of difficult proteins such as IMP-1, where the sequence-specific NMR resonance

500    assignments are incomplete due to line-broadening attributable to motions in the μs–ms time

501    range and additional signals are observed that either stem from protein degradation, misfolding

502    or alternative conformations in slow exchange with the main structure. Notably, all information

503    required to establish the $\Delta\chi$ tensors could be obtained from resolved cross-peaks observed in

504    sensitive [$^{15}$N,$^{1}$H]-HSQC spectra. Similarly, the localisation information of the tryptophan

505    sidechains could be obtained from sensitive $^{13}$C-$^{1}$H and $^{15}$N-$^{1}$H correlation spectra. Positioning

506    the lanthanoid tags relatively far from the substrate binding site avoided direct interference

507    with the binding loop structure.

508          In the face of additional signals from minor species, site-selective $^{13}$C-labelling of the

509    tryptophan sidechains was particularly helpful for simplifying the [$^{13}$C,$^{1}$H]-HSQC spectra.

510    Gratifyingly, this could be achieved by providing suitably labelled indole without having to

511    synthesise the full amino acid (Maleckis et al., 2021).

512          It has been pointed out previously that the accuracy with which localisation spaces can

513    be determined is best when PCS isosurfaces intersect in an orthogonal manner (Pintacuda et

514    al., 2006; Lescanne et al., 2018; Zimmermann et al., 2019). In the present work, we found that,

515    counterintuitively, the provision of additional data can considerably degrade the accuracy of

516    the localisation space. This effect arises when PCS isosurfaces intersect at a shallow angle, as

517    the location of these intersections becomes very sensitive with regard to small errors in the

518    relative orientations of the underpinning $\Delta\chi$ tensors. Shallow intersection angles of PCS

519    isosurfaces are common, when two PCS datasets are from tags and tagging sites that differ only

520    in the identity of the paramagnetic metal ion in the tag. This situation commonly generates $\Delta\chi$

521    tensors of different magnitude and sign, but closely similar orientation (Bertini et al., 2001; Su

522    et al., 2008; Keizers et al., 2008; Man et al., 2010; Graham et al., 2011; Joss et al., 2018;

523    Zimmermann et al., 2021). Therefore, while the use of Tm$^{3+}$ and Tb$^{3+}$ tags is helpful for

524    assigning the cross-peaks in the paramagnetic state, more robust results are obtained by using

525    only one of these data sets for calculating the localisation space. Good localisation spaces were

526    thus obtained by using only PCSs measured for Tb$^{3+}$ tags (Fig. 6) or only PCSs measured for

527    Tm$^{3+}$ tags (Fig. S13). In contrast, however, very different tags attached at the same site, such

528 as the C2 and C12 tags installed in the mutant N172C, produced independent $\Delta\chi$-tensor

529 orientations and therefore contributed positively to localising the Trp28 H$^{\varepsilon 1}$ atom.

530       In principle it is inappropriate to explain a set of PCSs by a single $\Delta\chi$ tensor, if they are

531 generated by a lanthanoid tag attached via a flexible linker, which positions the lanthanide ions

532 at variable coordinates relative to the protein. In this situation, fitting a single $\Delta\chi$ tensor

533 amounts to an approximation. The effective $\Delta\chi$ tensors obtained in this way, however, can

534 fulfill the PCSs remarkably well (Shishmarev and Otting, 2013), as illustrated by the low $Q$

535 factors obtained in this work (Fig. 4), and the localisation spaces obtained for the tryptophan

536 sidechains are correspondingly well defined.

537       The present work employed $^1$H PCSs only, although PCSs were also observed in the

538 indirect dimensions of the [$^{13}$C,$^1$H]-HSQC and [$^{15}$N,$^1$H]-HSQC spectra. We made this choice

539 because the paramagnetic tags give rise to weak molecular alignments in the magnetic field,

540 which result in residual anisotropic chemical shifts (RACS). The effect is unimportant for $^1$H

541 spins but significant for nuclear spins with large chemical shift anisotropy (CSA) tensors such

542 as backbone nitrogens and aromatic carbons. Correcting for the RACS effect is possible with

543 prior knowledge of the CSA tensors and bond orientations (John et al., 2005). We therefore

544 chose not to measure PCSs of the heteronuclear spins in favour of improving sensitivity by

545 accepting a lower spectral resolution in the indirect dimensions.

546       Finally, the C12 tag was designed specifically with the intent to produce a more rigid

547 tether to the protein than the C2 tag, but this did not result in larger $\Delta\chi$ tensors (Table S7) and

548 the NMR spectra of IMP-1 N172C displayed more heterogeneity with the C12 than the C2 tag,

549 suggesting that the shorter and more rigid tether combined with the fairly high molecular

550 weight of the cyclen-lanthanoid complex may have perturbed the protein structure to some

551 degree.

552

553 **5 Conclusion**

554 The current work illustrates how $\Delta\chi$ tensors from paramagnetic lanthanoid ion tags installed at

555 three different sites of the protein can be used to probe the conformation of a selected site in

556 solution in unprecedented detail, provided the structure of most of the protein is known with

557 high accuracy to allow fitting effective $\Delta\chi$ tensors of high predictive value. Importantly,

558 however, the method is easily compromised, if two PCS isosurfaces intersect at a shallow angle

559 as, in this situation, inaccuracies in $\Delta\chi$ tensor determinations have an outsized effect on

560 positioning the localisation spaces defined by the PCSs. Therefore, improved results were

561    obtained by not combining data from different metal ions bound to otherwise identical tags and

562    tagging sites. In the present work, simplifying the NMR spectrum of tryptophan residues by

563    site-selective isotope labelling proved to be of great value for sufficiently improving the

564    spectral resolution to allow assigning the labelled resonances solely from PCSs and PREs. The

565    strategy opens a path to detailed structural investigations of proteins of limited stability like

566    IMP-1, for which complete assignments of the NMR spectrum are difficult to obtain.

567

568

590

591     **References**

592    Arakawa, Y., Murakami, M., Suzuki, K., Ito, H., Wacharotayankun, R., Ohsuka, S., Kato, N.,

593        and Ohta, M.: A novel integron-like element carrying the metallo-β-lactamase gene $bla_{IMP}$,

594  Antimicrob. Agents Chemother., 39, 1612–1615, https://doi.org/10.1128/AAC.39.7.1612,
595  1995.

596  Bertini, I., Janik, M. B. L., Lee, Y. M., Luchinat, C., and Rosato, A.: Magnetic susceptibility
597  tensor anisotropies for a lanthanide ion series in a fixed protein matrix, J. Am. Chem. Soc.,
598  123, 4181–4188, https://doi.org/10.1021/ja0028626, 2001.

599  Brem, J., van Berkel, S. S., Zollman, D., Lee, S. Y., Gileadi, O., McHugh, P. J., Walsh, T. R.,
600  McDonough, M.A., and Schofield, C. J.: Structural basis of metallo-β-lactamase inhibition
601  by captopril stereoisomers, Antimicrob. Agents Chemother., 60, 142–150,
602  https://doi.org/10.1128/AAC.01335-15, 2016.

603  Brewer, K. D., Bacaj, T., Cavalli, A., Camilloni, C., Swarbrick, J. D., Liu, J., Zhou, A., Zhou,
604  P., Barlow, N., Xu, J., Seven, A. B., Prinslow, E. A., Voleti, R., Häussinger, D., Bonvin, A.
605  M. J. J., Tomchick, D. R., Vendruscolo, M., Graham, B., Südhof, T. C., and Rizo, J.:
606  Dynamic binding mode of a synaptotagmin-1-SNARE complex in solution, Nat. Struct.
607  Mol. Biol., 22, 555–564, https://doi.org/10.1038/nsmb.3035, 2015.

608  Bush, K.: Proliferation and significance of clinically relevant β-lactamases, Ann. N. Y. Acad.
609  Sci., 1277, 84−90, https://doi.org/10.1111/nyas.12023, 2013.

610  Bush, K.: Alarming β-lactamase-mediated resistance in multidrug-resistant
611  *Enterobacteriaceae*, Curr. Opin. Microbiol., 13, 558−564,
612  https://doi.org/10.1016/j.mib.2010.09.006, 2010.

613  Carruthers, T. J.: Paramagnetism & Structural Biology: Biochemical & Biophysical Analysis
614  of IMP-1 Metallo-β-lactamase, PhD thesis, The Australian National University, Canberra,
615  221 pp., 2014.

616  Carruthers, T. J., Carr, P. D., Loh, C.-T., Jackson, C. J., and Otting, G.: $Fe^{3+}$ located in the
617  dinuclear metallo-β-lactamase IMP-1 by pseudocontact shifts, Angew. Chemie Int. Ed., 53,
618  14269−14272, https://doi.org/10.1002/anie.201408693, 2014.

619  Chen, W.-N., Nitsche, C., Pilla, K. B., Graham, B., Huber, T., Klein, C. D., and Otting, G.:
620  Sensitive NMR approach for determining the binding mode of tightly binding ligand
621  molecules to protein targets, J. Am. Chem. Soc., 138, 4539−4546,
622  https://doi.org/10.1021/jacs.6b00416, 2016.

623  Concha, N. O., Rasmussen, B. A., Bush, K., and Herzberg, O.: Crystal structure of the wide-
624  spectrum binuclear zinc β-lactamase from *Bacteroides fragilis*, Structure, 4, 823–836,
625  https://doi.org/10.1016/S0969-2126(96)00089-5, 1996.

626 Concha, N. O., Janson, C. A., Rowling, P., Pearson, S., Cheever, C. A., Clarke, B. P., Lewis,
627 C., Galleni, M., Frere, J.-M., Payne, D. J., Bateson, J. H., and Abdel-Meguid, S. S.: Crystal
628 Structure of the IMP-1 metallo-β-lactamase from *Pseudomonas aeruginosa* and its complex
629 with a mercaptocarboxylate inhibitor: binding determinants of a potent, broad-spectrum
630 inhibitor, Biochemistry, 39, 4288–4298, https://doi.org/10.1021/bi992569m, 2000.

631 Crick, D. J., Wang, J. X., Graham, B., Swarbrick, J. D., Mott, H. R., and Nietlispach, D.:
632 Integral membrane protein structure determination using pseudocontact shifts, J. Biomol.
633 NMR, 61, 197–207, https://doi.org/10.1007/s10858-015-9899-6, 2015.

634 de la Cruz, L., Nguyen, T.H.D., Ozawa, K., Shin, J., Graham, B., Huber, T., and Otting, G.:
635 Binding of low-molecular weight inhibitors promotes large conformational changes in the
636 dengue virus NS2B-NS3 protease: fold analysis by pseudocontact shifts, J. Am. Chem. Soc.,
637 133, 19205–19215, https://doi.org/10.1021/ja208435s, 2011.

638 Galleni, M., Lamotte-Brasseur, J., Rossolini, G. M., Spencer, J., Dideberg, O., Frère, J.-M.,
639 and The Metallo-β-Lactamase Working Group: Standard numbering scheme for class B β-
640 lactamases. Antimicrob. Agents Chemother., 45, 660–663,
641 https://doi.org/10.1128/AAC.45.3.660-663.2001, 2001.

642 Gianquinto, E., Tondi, D., D'Arrigo, G., Lazzarato, L., and Spyrakis, F.: Can we exploit β-
643 lactamases intrinsic dynamics for designing more effective inhibitors? Antibiotics, 9, 833,
644 https://doi.org/10.3390/antibiotics9110833, 2020.

645 González, M. M., Abriata, L. A., Tomatis, P. E., and Vila, A. J.: Optimization of
646 conformational dynamics in an epistatic evolutionary trajectory, Mol. Biol. Evol., 33, 1768–
647 1776, https://doi.org/10.1093/molbev/msw052, 2016.

648 Graham, B., Loh, C.T., Swarbrick, J.D., Ung, P., Shin, J., Yagi, H., Jia, X., Chhabra, S.,
649 Pintacuda, G., Huber, T., and Otting, G.: A DOTA-amide lanthanide tag for reliable
650 generation of pseudocontact shifts in protein NMR spectra, Bioconjugate Chem., 22, 2118–
651 2125, https://doi.org/10.1021/bc200353c, 2011.

652 Guan, J. Y., Keizers, P. H. J., Liu, W. M., Löhr, F., Skinner, S. P., Heeneman, E. A., Schwalbe,
653 H., Ubbink, M., and Siegal, G.: Small-molecule binding sites on proteins established by
654 paramagnetic NMR spectroscopy. J. Am. Chem. Soc., 135, 5859–5868,
655 https://doi.org/10.1021/ja401323m, 2013.

656 Herath, I. D., Breen, C., Hewitt, S. H., Berki, T. R., Kassir, A. F., Dodson, C., Judd, M., Jabar,
657 S., Cox, N., Otting, G., and Butler, S. J.: A chiral lanthanide tag for stable and rigid
658 attachment to single cysteine residues in proteins for NMR, EPR and time-resolved

659  luminescence studies, Chem. Eur. J., 27, 13009–13023,
660  https://doi.org/10.1002/chem.202101143, 2021.

661  Hinchliffe, P., González, M. M., Mojica, M. F., González, J. M., Castillo, V., Saiz, C.,
662  Kosmopoulou, M., Tooke, C. L., Llarrull, L. I., Mahler, G., and Bonomo, R. A.: Cross-class
663  metallo-β-lactamase inhibition by bisthiazolidines reveals multiple binding modes, Proc.
664  Nat. Acad. Sci., 113, E3745–E3754, https://doi.org/10.1073/pnas.1601368113, 2016.

665  Hinchliffe, P., Tanner, C. A., Krismanich, A. P., Labbé, G., Goodfellow, V. J., Marrone, L.,
666  Desoky, A. Y., Calvopiña, K., Whittle, E. E., Zeng, F., and Avison, M. B.: Structural and
667  kinetic studies of the potent inhibition of metallo-β-lactamases by 6-
668  phosphonomethylpyridine-2-carboxylates, Biochemistry, 57, 1880–1892,
669  https://doi.org/10.1021/acs.biochem.7b01299, 2018.

670  Hiraiwa, Y., Saito, J., Watanabe, T., Yamada, M., Morinaka, A., Fukushima, T., and Kudo, T.:
671  X-ray crystallographic analysis of IMP-1 metallo-β-lactamase complexed with a 3-
672  aminophthalic acid derivative, structure-based drug design, and synthesis of 3,6-
673  disubstituted phthalic acid derivative inhibitors, Bioorg. Med. Chem. Lett., 24, 4891–4894,
674  https://doi.org/10.1016/j.bmcl.2014.08.039, 2014.

675  Huntley, J.J.A., Scrofani, S.D.B., Osborne, M.J., Wright, P.E., and Dyson, H.J.: Dynamics of
676  the metallo-β-lactamase from *Bacteroides fragilis* in the presence and absence of a tight-
677  binding inhibitor, Biochemistry, 39, 13356–13364, https://doi.org/10.1021/bi001210r,
678  2000.

679  Huntley, J. J. A., Fast, W., Benkovic, S. J., Wright, P. E., and Dyson, H. J.: Role of a solvent-
680  exposed tryptophan in the recognition and binding of antibiotic substrates for a metallo-β-
681  lactamase, Protein Sci., 12, 1368–1375, https://doi.org/10.1110/ps.0305303, 2003.

682  Ito, H., Arakawa, Y., Ohsuka, S., Wachorotayankun, R., Kato, N., and Ohta, M.: Plasmid-
683  mediated dissemination of the metallo-β-lactamase gene *bla*IMP among clinically isolated
684  strains of *Serratia marcescens*, Antimicrob. Agents Chemother., 39, 824–829,
685  https://doi.org/10.1128/AAC.39.4.824, 1995.

686  John, M., Park, A. Y., Pintacuda, G., Dixon, N. E., and Otting, G.: Weak alignment of
687  paramagnetic proteins warrants correction for residual CSA effects in measurements of
688  pseudocontact shifts, J. Am. Chem. Soc., 127, 17190–17191,
689  https://doi.org/10.1021/ja0564259, 2005.

690  John, M., Park, A. Y., Pintacuda, G., Dixon, N. E., and Otting, G.: Weak alignment of
691  paramagnetic proteins warrants correction for residual CSA effects in measurements of

pseudocontact shifts, J. Am. Chem. Soc., 127, 17190–17191, https://doi.org/10.1021/ja0564259, 2005.

Joss, D., Walliser, R. M., Zimmermann, K., and Häussinger, D.: Conformationally locked lanthanide chelating tags for convenient pseudocontact shift protein nuclear magnetic resonance spectroscopy, J. Biomol. NMR, 72, 29–38, https://doi.org/10.1007/s10858-018-0203-4, 2018.

Keizers, P. H. J., Saragliadis, A., Hiruma, Y., Overhand, M., and Ubbink, M.: Design, synthesis, and evaluation of a lanthanide chelating protein probe: CLaNP-5 yields predictable paramagnetic effects independent of environment, J. Am. Chem. Soc., 130, 14802–14812, https://doi.org/10.1021/ja8054832, 2008.

Keizers, P. H. J., Mersinli, B., Reinle, W., Donauer, J., Hiruma, Y., Hannemann, F., Overhand, M., Bernhardt, R., and Ubbink, M.: A solution model of the complex formed by adrenodoxin and adrenodoxin reductase determined by paramagnetic NMR spectroscopy, Biochemistry, 49, 6846–6855, https://doi.org/10.1021/bi100598f, 2010.

Kobashigawa, Y., Saio, T., Ushio, M., Sekiguchi, M., Yokochi, M., Ogura, K., and Inagaki, F.: Convenient method for resolving degeneracies due to symmetry of the magnetic susceptibility tensor and its application to pseudo contact shift-based protein-protein complex structure determination, J. Biomol. NMR, 53, 53–63, https://doi.org/10.1007/s10858-012-9623-8, 2012.

Laraki, N., Galleni, M., Thamm, I., Riccio, M. L., Amicosante, G., Frère, J.-M., and Rossolini, G. M.: Structure of In101, a $bla_{IMP}$-containing *Pseudomonas aeruginosa* integron phyletically related to In5, which carries an unusual array of gene cassettes, Antimicrob. Agents Chemother., 43, 890–901, https://doi.org/10.1128/AAC.43.4.890, 1999a.

Laraki, N., Franceschini, N., Rossolini, G. M., Santucci, P., Meunier, C., De Pauw, E., Amicosante, G., Frère, J.-M., and Galleni, M.: Biochemical characterization of the *Pseudomonas aeruginosa* 101/1477 metallo-β-lactamase IMP-1 produced by *Escherichia coli*, Antimicrob. Agents Chemother., 43, 902–906, https://doi.org/10.1128/AAC.43.4.902, 1999b.

Lescanne, M., Ahuja, P., Blok, A., Timmer, M., Akerud, T., and Ubbink, M.: Methyl group reorientation under ligand binding probed by pseudocontact shifts, J. Biomol. NMR, 71, 275–285, https://doi.org/10.1007/s10858-018-0190-5, 2018.

723 Linciano, P., Cendron, L., Gianquinto, E., Spyrakis, F., and Tondi, D.: Ten years with New
724 Delhi metallo-β-lactamase-1 (NDM-1): from structural insights to inhibitor design, ACS
725 Infect. Dis. 5, 9–34, https://doi.org/10.1021/acsinfecdis.8b00247, 2018.

726 Maleckis, A., Herath, I. D., and Otting, G.: Synthesis of $^{13}C/^{19}F/^{2}H$ labeled indoles for use as
727 tryptophan precursors for protein NMR spectroscopy, Org. Biomol. Chem., 19, 5133–5147,
728 https://doi.org/10.1039/D1OB00611H, 2021.

729 Man, B., Su, X.-C., Liang, H., Simonsen, S., Huber, T., Messerle, B. A., and Otting, G.: 3-
730 Mercapto-2,6-pyridinedicarboxylic acid, a small lanthanide-binding tag for protein studies
731 by NMR spectroscopy, Chem. Eur. J., 16, 3827–3832,
732 https://doi.org/10.1002/chem.200902904, 2010.

733 Markley, J. L., Bax, A., Arata, Y., Hilbers, C. W., Kaptein, R., Sykes, B. D., Wright, P. E., and
734 Wüthrich, K.: Recommendations for the presentation of NMR structures of proteins and
735 nucleic acids - IUPAC-IUBMB-IUPAB Inter-Union Task Group on the Standardization of
736 Data Bases of Protein and Nucleic Acid Structures Determined by NMR Spectroscopy, J.
737 Biomol. NMR, 12, 1–23, https://doi.org/10.1023/A:1008290618449, 1998.

738 Meissner, A., Duus, J. Ø., and Sørensen, O. W.: Spin-state-selective excitation. Application for
739 E.COSY-type measurement of $J_{HH}$ coupling constants, J. Magn. Reson., 128, 92–97,
740 https://doi.org/10.1006/jmre.1997.1213, 1997.

741 Moali, C., Anne, C., Lamotte-Brasseur, J., Groslambert, S., Devreese, B., Van Beeumen, J.,
742 Galleni, M., and Frère, J.M.: Analysis of the importance of the metallo-β-lactamase active
743 site loop in substrate binding and catalysis, Chemistry & Biology, 10, 319–329,
744 https://doi.org/10.1016/S1074-5521(03)00070-X, 2003.

745 Orton, H. W., Huber, T., and Otting, G.: Paramagpy: software for fitting magnetic
746 susceptibility tensors using paramagnetic effects measured in NMR spectra, Magn.
747 Reson., 1, 1–12, https://doi.org/10.5194/mr-1-1-2020, 2020.

748 Palacios, A. R, Mojica, M. F., Giannini, E., Taracila, M. A., Bethel, C. R., Alzari, P. M., Otero,
749 L. H., Klinke, S., Llarrull, L. I., Bonomo, R. A., and Vila, A. J.: The reaction mechanism of
750 metallo-β-lactamases is tuned by the conformation of an active-site mobile loop,
751 Antimicrob. Agents Chemother, 63, e01754-18, https://doi.org/10.1128/AAC.01754-18,
752 2019.

753 Payne, D. J., Hueso-Rodriguez, J. A., Boyd, H., Concha, N. O., Janson, C. A., Gilpin, M.,
754 Bateson, J. H., Cheever, C., Niconovich, N. L., Pearson, S., Rittenhouse, S., Tew, D., Díez,
755 E., Pérez, P., de la Fuente, J., Rees, M., and Rivera-Sagredo, A.: Identification of a series of

756    tricyclic natural products as potent broad-spectrum inhibitors of metallo-β-lactamases,

757    Antimicrob. Agents Chemother., 46, 1880–1886, https://doi.org/10.1128/AAC.46.6.1880-

758    1886.2002, 2002.

759    Pearce, B. J. G., Jabar, S., Loh, C. T., Szabo, M., Graham, B., and Otting, G.: Structure

760    restraints from heteronuclear pseudocontact shifts generated by lanthanide tags at two

761    different sites, J. Biomol. NMR, 68, 19–32, https://doi.org/10.1007/s10858-017-0111-z,

762    2017.

763    Pilla, K. B., Otting, G., and Huber, T.: Protein structure determination by assembling super-

764    secondary structure motifs using pseudocontact shifts, Structure, 25, 559–568,

765    https://doi.org/10.1016/j.str.2017.01.011, 2017.

766    Pintacuda, G., Park, A. Y., Keniry, M. A., Dixon, N. E., and Otting, G.: Lanthanide labeling

767    offers fast NMR approach to 3D structure determinations of protein-protein complexes, J.

768    Am. Chem. Soc., 128, 3696–3702, https://doi.org/10.1021/ja057008z, 2006.

769    Rossi, M.-A., Martinez, V., Hinchliffe, P., Mojica, M. F., Castillo, V., Moreno, D. M., Smith,

770    R., Spellberg, B., Drusano, G. L., Banchio, C., Bonomo, R. A., Spencer, J., Vila, A. J., and

771    Mahler, G.: 2-Mercaptomethyl-thiazolidines use conserved aromatic–S interactions to

772    achieve broad-range inhibition of metallo-β-lactamases, Chem. Sci., 12, 2898–2908,

773    https://doi.org/10.1039/d0sc05172a, 2021.

774    Salimraj, R., Hinchliffe, P., Kosmopoulou, M., Tyrrell, J. M., Brem, J., van Berkel, S. S.,

775    Verma, A., Owens, R. J., McDonough, M. A., Walsh, T. R., Schofield, C. J., and Spencer,

776    J.: Crystal structures of VIM-1 complexes explain active site heterogeneity in VIM-class

777    metallo-β-lactamases, FEBS J., 286, 169–183, https://doi.org/10.1111/febs.14695, 2018.

778    Shishmarev, D. and Otting, G.: How reliable are pseudocontact shifts induced in proteins and

779    ligands by mobile paramagnetic metal tags? A modelling study, J. Biomol. NMR, 56, 203–

780    216, https://doi.org/10.1007/s10858-013-9738-6, 2013.

781    Softley, C. A., Zak, K. M., Bostock, M. J., Fino, R., Zhou, R. X., Kolonko, M., Mejdi-Nitiu,

782    R., Meyer, H., Sattler, M., and Popowicz, G. M.: Structure and molecular recognition

783    mechanism of IMP-13 metallo-β-lactamase, Antimicrob. Agents Chemother., 64, e00123-

784    20, https://doi.org/10.1128/AAC.00123-20, 2020.

785    Su, X.-C., McAndrew, K., Huber, T., and Otting, G.: Lanthanide-binding peptides for NMR

786    measurements of residual dipolar couplings and paramagnetic effects from multiple angles,

787    J. Am. Chem. Soc., 130, 1681–1687, https://doi.org/10.1021/ja076564l, 2008.

788 Toney, J. H., Hammond, G. G., Fitzgerald, P. M., Sharma, N., Balkovec, J. M., Rouen, G. P.,
789 Olson, S. H., Hammond, M. L., Greenlee, M. L., and Gao, Y. D.: Succinic acids as potent
790 inhibitors of plasmid-borne IMP-1 metallo-β-lactamase, J. Biol. Chem., 276, 31913–31918,
791 https://doi.org/10.1074/jbc.M104742200, 2001.

792 van Duin, D., Kaye, K. S., Neuner, E. A., and Bonomo, R. A.: Carbapenem-resistant
793 Enterobacteriaceae: a review of treatment and outcomes, Diagn. Microbiol. Infect. Dis. 75,
794 115−120, https://doi.org/10.1016/j.diagmicrobio.2012.11.009, 2013.

795 Wachino, J., Kanechi, R., Nishino, E., Mochizuki, M., Jin, W., Kimura, K., Kurosaki, H., and
796 Arakawa, Y.: 4-Amino-2-sulfanylbenzoic acid as a potent subclass B3 metallo-β-lactamase-
797 specific inhibitor applicable for distinguishing metallo-β-lactamase subclasses, Antimicrob.
798 Agents Chemother. 63, e01197-19, https://doi.org/10.1128/AAC.01197-19, 2019.

799 Watanabe, M., S. Iyobe, M. Inoue, and S. Mitsuhashi: Transferable imipenem resistance in
800 *Pseudomonas aeruginosa*, Antimicrob. Agents Chemother. 35, 147–151, https://doi.org/
801 10.1128/AAC.35.1.147, https://doi.org/10.1128/AAC.35.1.147, 1991.

802 Yagi, H., Pilla, K. B., Maleckis, A., Graham, B., Huber, T., and Otting, G.: Three-dimensional
803 protein fold determination from backbone amide pseudocontact shifts generated by
804 lanthanide tags at multiple sites, Structure, 21, 883–890,
805 https://doi.org/10.1016/j.str.2013.04.001, 2013.

806 Yamaguchi, Y., Matsueda, S., Matsunaga, K., Takashio, N., Toma-Fukai, S., Yamagata, Y.,
807 Shibata, N., Wachino, J., Shibayama, K., Arakawa, Y., and Kurosaki, H.: Crystal structure
808 of IMP-2 metallo-β-lactamase from *Acinetobacter* spp.: comparison of active-site loop
809 structures between IMP-1 and IMP-2, Biol. Pharm. Bull. 38, 96–
810 101, https://doi.org/10.1248/bpb.b14-00594, 2015.

811 Yamaguchi, Y., Kato, K., Ichimaru, Y., Jin, W., Sakai, M., Abe, M., Wachino, J., Arakawa,
812 Y., Miyagi, Y., Imai, M., Fukuishi, N., Yamagata, Y., Otsuka, M., Fujita, M., and Kurosaki,
813 H.: Crystal structures of metallo-β-lactamase (IMP-1) and its D120E mutant in complexes
814 with citrate and the inhibitory effect of the benzyl group in citrate monobenzyl ester, J. Med.
815 Chem., 64, 10019–10026, https://doi.org/10.1021/acs.jmedchem.1c00308, 2021.

816 Yamaguchi, H., M. Nukaya, and T. Sawai, T: Sequence of *Klebsiella pneumoniae* RDK4
817 metallo-β-lactamase, EMBO database accession no. D29636, EMBO, Heidelberg,
818 Germany, 1994.

819 Zimmermann, K., Joss, D., Müntener, T., Nogueira, E. S., Schäfer, M., Knörr, L., Monnard,
820 F. W., and Häussinger, D.: Localization of ligands within human carbonic anhydrase II

821 using $^{19}$F pseudocontact shift analysis, Chem. Sci., 10, 5064–5072,

822 https://doi.org/10.1039/c8sc05683h, 2019.